High-resolution FIB-TEM-STEM structural characterization of grain boundaries in the high dielectric constant perovskite CaCu3Ti4O12

Bernadette Domengès, Guillaume Riquet, Sylvain Marinel, Christelle Harnois

▶ **To cite this version:**

HAL Id: hal-02533305

https://normandie-univ.hal.science/hal-02533305

Submitted on 7 Jan 2021

High-resolution FIB-TEM-STEM structural characterization of grain boundaries in the high dielectric constant perovskite $CaCu_3Ti_4O_{12}$

Bernadette DOMENGES*, Guillaume RIQUET, Sylvain MARINEL, Christelle HARNOIS

Laboratoire de Cristallographie et Science des Matériaux, Normandie Univ, ENSICAEN, UNICAEN, CNRS, CRISMAT, 14000 Caen, France

*: Corresponding author

E-mail address: bernadette.domenges@ensicaen.fr

Postal address : Laboratoire CRISMAT, 6 Boulevard du Maréchal Juin, 14050 CAEN Cedex 4, France

Abstract

In this work, the grain boundaries composition of the polycrystalline $CaCu_3Ti_4O_{12}$ (CCTO) was investigated. A Focused Ion Beam (FIB)/lift-out technique was used to prepare site-specific thin samples of the grain boundaries interface of CCTO ceramics. Scanning transmission electron microscopy (STEM) coupled with energy dispersive X-ray spectrometry (EDXS) and Electron Energy Loss Spectroscopy (EELS) systems were used to characterize the composition and nanostructure of the grain and grain boundaries region. It is known that during conventional sintering, discontinuous grain growth occurs and a Cu-rich phase appears at grain boundaries. This Cu-rich phase may affect the final dielectric properties of CCTO but its structure and chemical composition remained unknown. For the first time, this high-resolution FIB-TEM-STEM study of CCTO interfacial region highlights the composition of the phases segregated at grain boundaries namely CuO, Cu_2O and the metastable phase Cu_3TiO_4.

1. Introduction

In the last years, the research of materials having high dielectric constant with good temperature stability has raised significant attention because of their numerous potential applications. Since the discovery by Subramanian *et al.* of high relative permittivity ($\varepsilon_r \approx 10^5$ at 1kHz, 25°C) in $CaCu_3Ti_4O_{12}$ (CCTO), stable on a wide temperature range [100K, 400K], CCTO has attracted much attention [1-3].

CCTO is a cubic double distorted perovskite-like structure where the Jahn Teller effect brings the cations Cu^{2+} site to a nearly square environment instead of the usual cubo-octahedral environment on the A site of the perovskite, inducing the tilt of TiO_6 octahedra (SG $Im\overline{3}$; a = 7.393 Å). According to the structure analysis, neither structural nor ferroelectric transition was observed in CCTO [4-6]. Shortly after the reports of those properties, the origin of the colossal dielectric constant has been questioned and arguments have been put forth that extrinsic effects might be the sources of this giant dielectric constant. The internal barrier layer capacitor (IBLC) model is now widely accepted to explain the giant capacitance behavior in CCTO ceramics [7-10]. Based on this model, a general guidance in interpreting the dielectric response of materials consisting of semi-conducting grains and insulating grain boundaries is provided by [11]:

$$\varepsilon_r \approx \varepsilon_{GB} \frac{A}{t} \tag{1}$$

The relative permittivity may be estimated from the dielectric constant of the insulating layers (ε_{GB}), the average grain size of semi-conducting grains (A) and the average thickness of grain boundaries (t). According to equation (1), if a high A/t ratio can be achieved by tuning the grains size and the thickness of grain boundaries, a material with an extremely high effective permittivity could be obtained [12,13]. Recently, Riquet *et al.* [14] studied the grain growth mechanism involved during conventional sintering process of CCTO. It appears that abnormal grain growth takes place for sintered samples at high temperature stage with density over 80% of the theoretical density (bulk density), making difficult the control of the microstructure. Besides, several works emphasized the segregation of Cu-rich phase at grain boundaries during sintering, supposed to be CuO or Cu_2O [14-17]. However, despite the importance the grain boundary composition may have on the dielectric properties of CCTO according to eq. (1), no precise structural characterization of grain boundary region in CCTO has been undertaken. For that purpose, it is therefore crucial to resort to characterization techniques at nano-structural scale such as High-Resolution Transmission and Scanning Transmission Electron Microscopy (HR-TEM-STEM) and related spectroscopy technics.

The aim of this paper is to characterize (structurally, chemically) at nanometric scale the nature of grain boundaries in CCTO ceramics, at least, in order to bring answers to the question, still unresolved at that time, of what type of copper rich phases were present at the grain boundaries.

2. Experimental procedure

2.1. Sample synthesis

The CCTO powder was obtained by conventional solid-state synthesis using highly pure $CaCO_3$ (99,95% Alfa Aesar), CuO (99,7% Alfa Aesar) and anatase-TiO_2 (99,9% Materion). Impurities of Si, K, P and Cr may be observed as trace levels in the starting materials. The precursors were mixed and grounded by ball milling during 16 min (using a Fritsch Pulverisette 6 planetary mill) with respect to the stoichiometry. Thereafter, the mixed precursor powder was heated three times in air in a tubular

furnace up to 900°C at 2.5°C.min^{-1} with a dwell of 10h. An organic binder (PVA - 1 wt%) was used to ensure a good cohesion of the compacted green samples. The CCTO powder was shaped into disks by uniaxial pressing at 5 MPa (6 mm in diameter, 6 mm thick) followed by an isostatic pressing step at 200 MPa. The binder was removed by a heat treatment in air at 400°C for 2h. The green sample density was 58 % of the theoretical value (5.05 g cm^{-3}). The sample was subsequently sintered in air up to 1100°C, at 2.5°C.min with a dwell time of 2h.

2.2. *Thin lamella preparation*

Among traditional electron-transparent -lamella preparation techniques, the Focused Ion Beam (FIB) one, based on a focused Ga$^+$ ion beam, is the one that allows site-specific TEM-sample preparations [18-19]. Moreover, Dual Beam (DB) systems, which associate scanning electron microscopy (SEM) and FIB, confirmed to be quite efficient to prepare the lamella at a grain boundary (GB) site. In order to ease the visualization of GBs, grinding and rough polishing of the sample surface were performed. Then, thin lamellae were prepared in a Dual-Beam system (FEI-HELIOS 600, Elstar Field Emission Scanning Electron Microscope column and Tomahawk Focused Ga Ion Beam column) equipped with Easy-lift manipulator designed for In-Situ Lift-Out thin lamella preparations [20]. The protective Pt-based bar was deposited in the DB as a rail across GBs and sometimes over an inclusion-like domain, as the one exhibiting a brighter contrast than that of the whole matrix in Fig. 1. Finally, lift-off In-situ technique was used to extract and prepare the thin lamella.
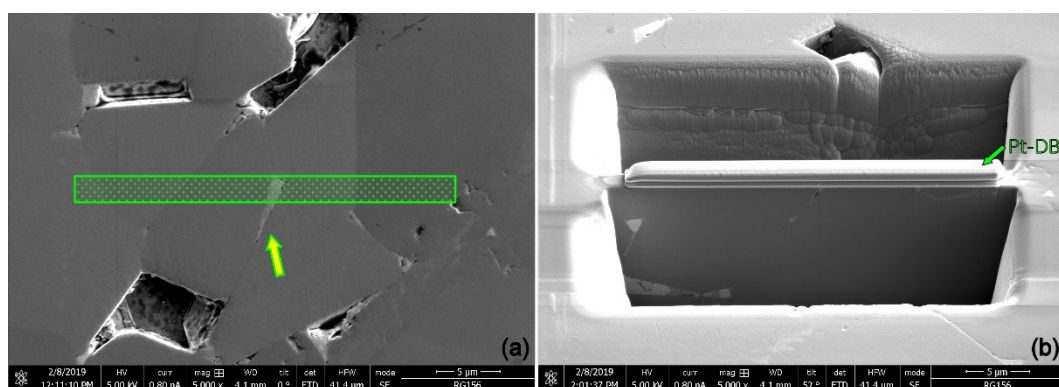

Fig. 1 (a) top-view DB-SEM image of the selected area of interest for the TEM lamella (speckled area), an inclusion-like domain is arrowed; (b) tilted view DB-SEM image of the lamella prior lift-off and thinning operations, Pt-based bar is arrowed (Pt-DB).

2.3. *Nanostructural Study*

Transmission Electron Microscopy (TEM) – Scanning Transmission Electron Microscopy (STEM) study was carried out on a JEM-ARM200F, operating at 200 kV, equipped with a cold FEG and double TEM-STEM Cs correctors, ensuring lattice TEM or STEM image resolution below 0.1 nm, and JEOL Energy Dispersive X-ray (EDX) spectrometry system (for concentration line profiles, the

electron nano-beam diameter is below 0.15 nm at the entrance surface of the lamella). The diameter of the selection aperture for Selected Area Electron Diffraction (SAED) patterns is 150 nm. Electron microscope is also equipped with Electron Energy Loss Spectroscopy (EELS) system (GATAN Quantum 965 ER DualEELS, 0.01 eV resolution). High Resolution Transmission Electron Miscroscopy (HRTEM) and High Angle Aperture Dark Field (HAADF)-STEM calculated images were obtained using JEMS program [21].

3. Results

Two TEM lamellae were prepared, one exhibiting a simple GB and the other including inclusions at the GB, so-called complex GB.

3.1. *Simple GB: nanostructural study*

First lamella was located across a simple GB between two large grains (Fig. 2(a)). The GB clearly appears on low magnification TEM image as a dark contrast line (Fig. 2(b)).
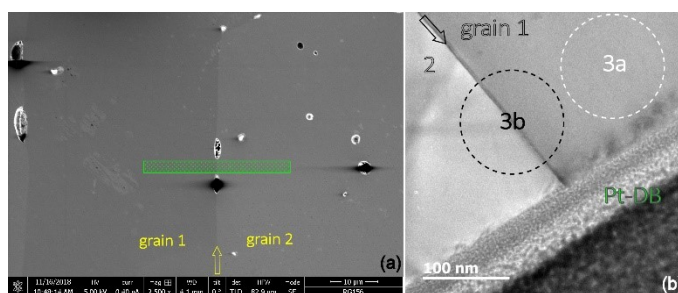

Fig. 2 (a) top view DB-SEM image of the selected area of interest for the TEM lamella (striped area), GB is arrowed; (b) medium resolution TEM image of the corresponding lamella showing the GB as a dark interface between grain 1 and 2; Pt-based bar exhibits an amorphous-like contrast (Pt-DB); circles visualize the position of the selected area aperture used for SAED patterns.

SAED study allowed to characterize the crystallographic relationships between the GB and the grains. Both grains were subsequently orientated with respect to the electron beam to obtain high symmetry SAED patterns (Fig. 3). On this lamella, {001} reciprocal plane could be aligned and observed. Main dots are indexed and follow the expected existence rules of $Im\overline{3}$ space group (*hk0, h+k=2n*). It does not seem that there is any correlation between grain orientations, with respect to each other and to the GB, which agrees with Electron Back Scattered Diffraction (EBSD) study showing no preferential orientation of the grains [22]. Furthermore, it appeared quite difficult to align the GB with the electron beam suggesting that it is not planar. Consequently, it exhibits on the HRTEM images an apparent width of a few nanometers, 2-3nm at optimum defocus value (Fig. 4).
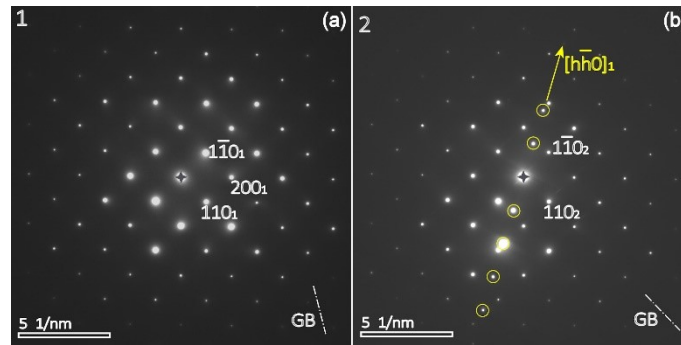
Fig. 3 SAED patterns of orientated grains, dotted line indicates the GB orientation. (a) grain 1 only is selected and orientated, $\{001\}_1^*$ reciprocal plane; (b) both grains are selected after orientation of grain 2, $\{001\}_2^*$ reciprocal plane, circled spots belong to grain 1, $< 1\bar{1}0 >_1^*$ reciprocal row.

Moiré patterns are observed on medium magnification HRTEM images at GB level, typical of superimposition of two crystallized domains (Fig. 4(a)). Observed contrast on high magnification image as compared with calculated image allowed to evaluate the thickness of the lamella of about 90nm, which is compatible with DualBeam preparation (Fig. 4(b)). Also, observed contrast at the GB suggests that no other framework than that of $CaCu_3Ti_4O_{12}$ is present. HRTEM cannot bring any more information on the GB, and HAADF-STEM was then used, allowing EDX analyses at nanometric scale.
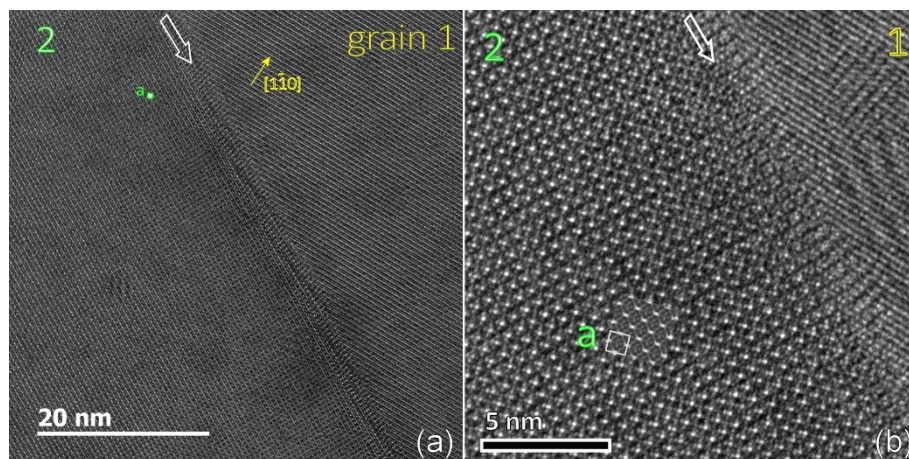

Fig. 4 High resolution TEM images taken with orientated grain 2, (a) medium magnification showing a GB apparent width of 2-3nm (white arrow),(b) high magnification with simulated image inserted (evaluated thickness is 90nm); unit cell is given on grain 2.

On HAADF-STEM images, high Z atom columns are highlighted. Along (001) projection for grain 2, the Cu and mixed Cu-Ca rows of the $CaCu_3Ti_4O_{12}$ framework appear as a square array of light grey dots (Fig. 5). At the same time, on grain 1, all atoms of (110) planes project onto each other and appear as light grey lines. At the GB, an abrupt change of contrast is observed, with no disorganized area at the interface.
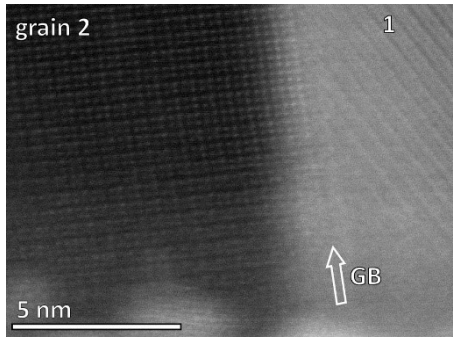
Fig. 5. HAADF-STEM image of thinner area of the lamella, showing no disordered interface at the GB.

EDX line profile was established on a thicker part of the GB, acquiring EDX spectra during 20s on each point of the line (Fig. 6). No significant increase of intensity of the CuK line was observed at the interface. Furthermore, traces of elements (Si, P, K) are detected; those are present in the synthesis precursors.
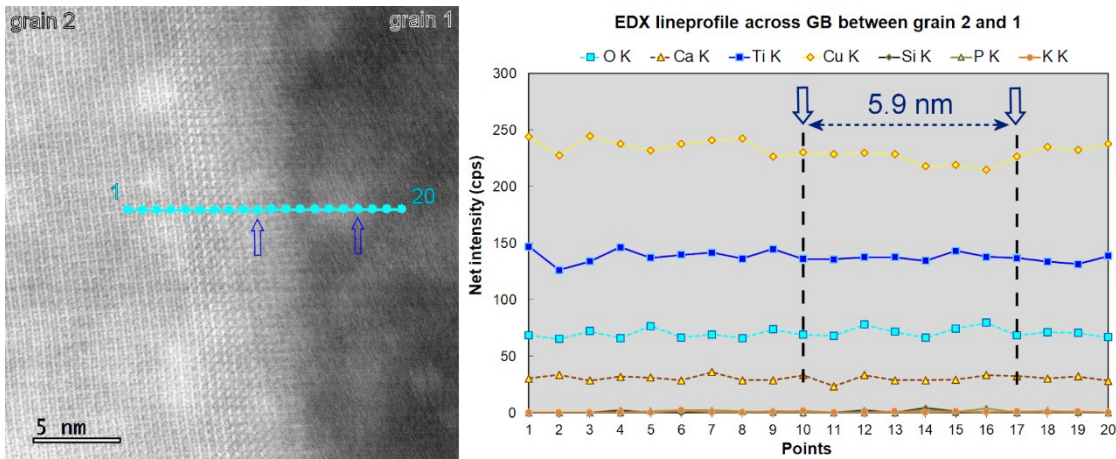

Fig. 6 HAADF-STEM image showing the location of the 20 points of EDX line profile across the GB; no significative variation of CuK line intensity is observed.

3.2. *Complex GB : nanostructural study*

The location of the second lamella can be seen on Fig. 1(a). From top view, it should allow to observe at least two simple GBs and a complex one. Once the thin lamella prepared, it appears that complex GBs sit at triple junction between grains (Fig. 7(a)). The observed contrasts on TEM image suggest that it is constituted of different domains, possibly of different nature (Fig. 7(b)).
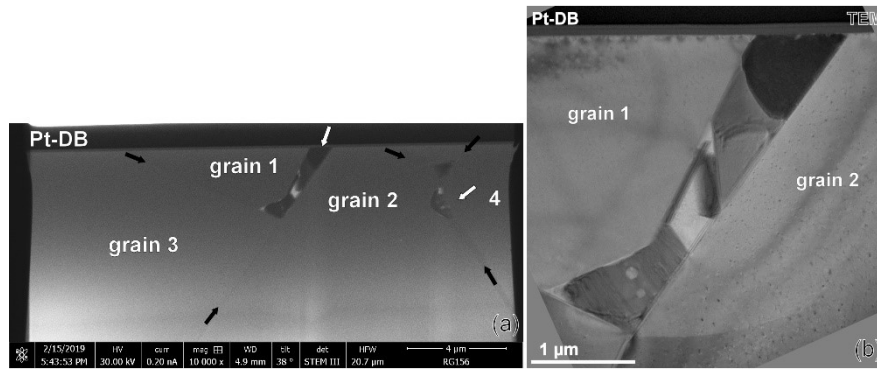
Fig. 7 (a) DB-STEM image of the thinned lamella before the final cleaning (thickness ~120nm). Complex GB (white arrows) are observed at the junction of several simple GBs (black arrows); (b) Corresponding TEM image of the biggest complex GB between grain 1, 2 and 3.

Correlative TEM-STEM analyses, based on SAED, HRTEM-STEM, and EDX technics allowed to clearly identify most of the different compounds stabilized at this complex GB. EDX analyses were performed in STEM mode and reliable quantitative atomic ratios could be obtained, as the lamella was supported on a Mo grid, contrary to usual Cu grids. This means that fluorescence effects will not affect the Cu line signals.

a. EDX analysis results

First, EDX line profile was performed across a GB between grains 1 and 3. In agreement with previous results, no increase in Cu ratio was observed (Fig. 8). As well, Si, P and K elements, precursors pollutants, were encountered, but in a slightly higher content, probably because this profile was taken close to the complex GB. The area of this analysis appears on medium resolution image of Fig. 9(a) as the small grey square.
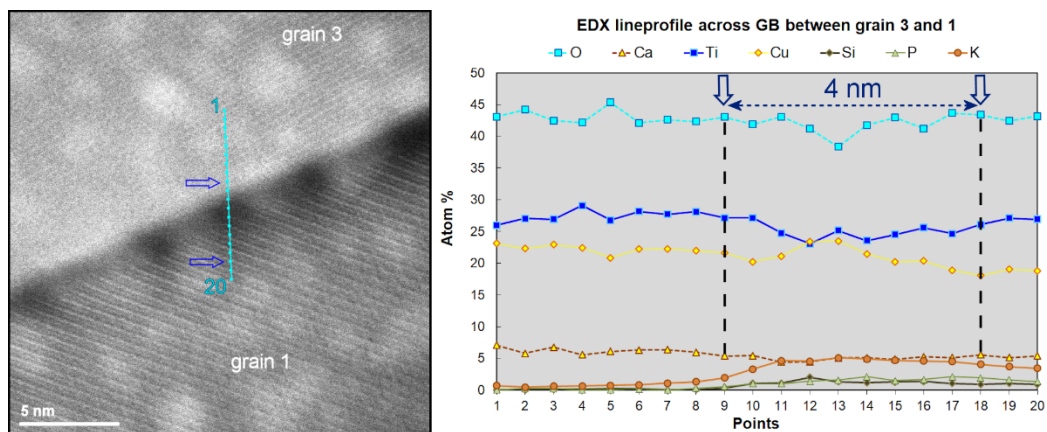

Fig. 8 HAADF-STEM image showing the location of the 20 points of EDS line profile across the GB between grain 3 and 1. Given atomic ratios were calculated based on O + Si + P + K + Ca + Ti + Cu = 100 %
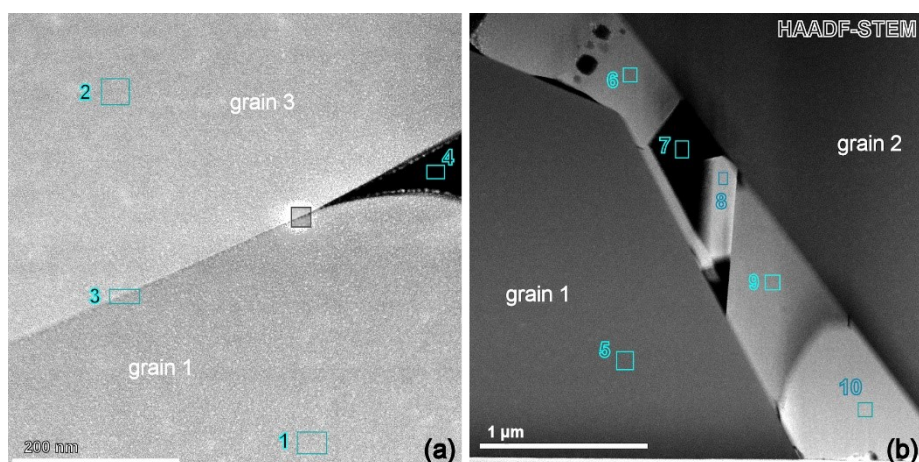
Fig. 9 HAADF-STEM images of the complex GB of Fig7, (a) medium resolution and (b) low resolution; the small rectangles figure out the area chosen for collecting the EDS spectra, and the small grey square in (a) gives the location of the area of interest for the previous line profile in Fig. 8.

Concerning grains and main domains of the complex GB, each EDS spectrum was collected from the different areas marked with a rectangle on the HAADF-STEM images of Fig. 9 and corresponding quantification results are given Table 1. On the medium resolution HAADF-STEM image (Fig. 9 (a)), four areas were analyzed. The dark contrast domain corresponds to amorphous area, containing light elements of the precursor pollutants and some Ti (area 4). The area across the GB does not exhibit any increase of Cu ratio. Two areas (6 and 9) do not contain any Ca, with a Cu/Ti ratio close to 3. Its formulation could be given as $Cu_{3-x}Ti_{1+y}O_z$.

Table 1 Atomic ratios observed on main areas of the complex GB

Area	Atomic % *							Identification
	O	Si	P	K	Ca	Ti	Cu	
1	42.1	0.0	0.1	0.0	7.3	28.2	22.3	$CaCu_3Ti_4O_{12}$
2	42.0	0.0	0.0	0.0	6.6	27.3	24.1	$CaCu_3Ti_4O_{12}$
3	41.7	0.2	0.0	0.3	6.0	28.4	23.5	$CaCu_3Ti_4O_{12}$
4	38.2	35.1	3.7	8.0	0.7	12.6	1.6	?
5	48.6	0.00	0.00	0.0	6.0	24.7	20.7	$CaCu_3Ti_4O_{12}$
6	44.3	0.2	0.1	0.1	0.0	14.0	41.3	Cu_3TiO_z
7	56.9	22.1	4.2	8.2	0.00	3.9	4.7	?
8	47.6	0.0	0.1	0.4	0.1	0.2	51.7	CuO
9	42.8	0.0	0.2	0.1	0.0	14.0	42.9	Cu_3TiO_z
10	31.6	0.3	0.0	0.0	0.1	0.1	67.9	Cu_2O

* Given atomic ratios were calculated based on O + Si + P + K + Ca + Ti + Cu = 100 %; this means that observed C lines (~6%) and fluorescence ones (Al, Fe, Co, Ga, Mo, Pt, which total ratio is below 11%), were considered but excluded from the quantification

On the low resolution HAADF-STEM image (b)), again the dark contrast domain contains only light elements of the precursor pollutants (area 7). Interestingly, two types of Cu-rich domains are observed CuO (area 8) and Cu_2O (area 10).

b. SAED study results

SAED study confirmed these observations. Some of the SAED patterns obtained after selecting and orientating some domains are given in Fig. 10. In agreement with EDS analyses, those corresponding to areas 5 and 10 could be respectively indexed in the $CaCu_3Ti_4O_{12}$ and Cu_2O frameworks. Both areas 6 and 9 are crystallized and based on their observed composition, the main dots of corresponding SAED pattern can be indexed in a distorted α-Cu_3TiO_4 framework (d_{010}=2.63Å), of delafossite-3R-type ($d_{003} = 5.75$Å, $d_{\bar{1}11} = 2.60$Å, $d_{012} = 2.52$Å)[22]. The diffuse streaks along the [001] direction suggest the presence of disordered stacking of the building layers that constitute the delafossite structure (ABO_2), which are sheets of linearly coordinated A cations stacked between edge-sharing octahedral layers (BO_2).

c. Delafossite-type domains

Domain 6 (Fig. 11) was further characterized using HR-TEM and HR-STEM imaging. It appeared that this domain was not homogeneous. Indeed, some areas, like area 1 of Fig. 12, exhibit a very regular stacking, as shown from the TEM image and the corresponding Fast Fourier Transform.
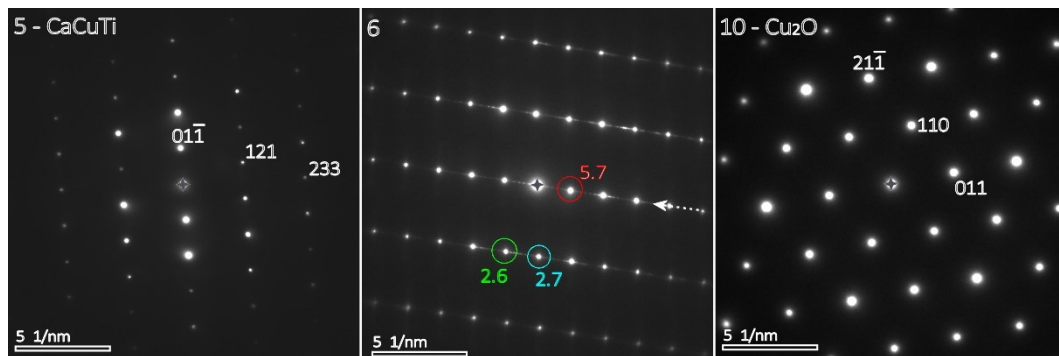

Fig. 10 SAED patterns obtained from areas 5, 6 and 10; for area 6, diffuse streaks can be seen along one direction (arrow), interreticular distances of main dots (circled) are given in angstrom.
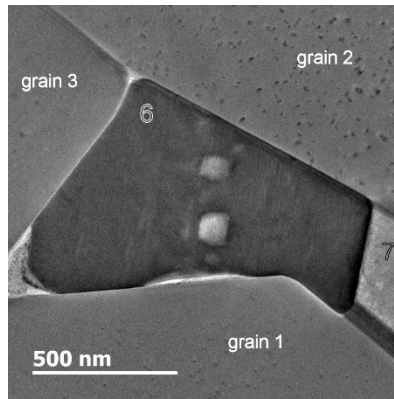
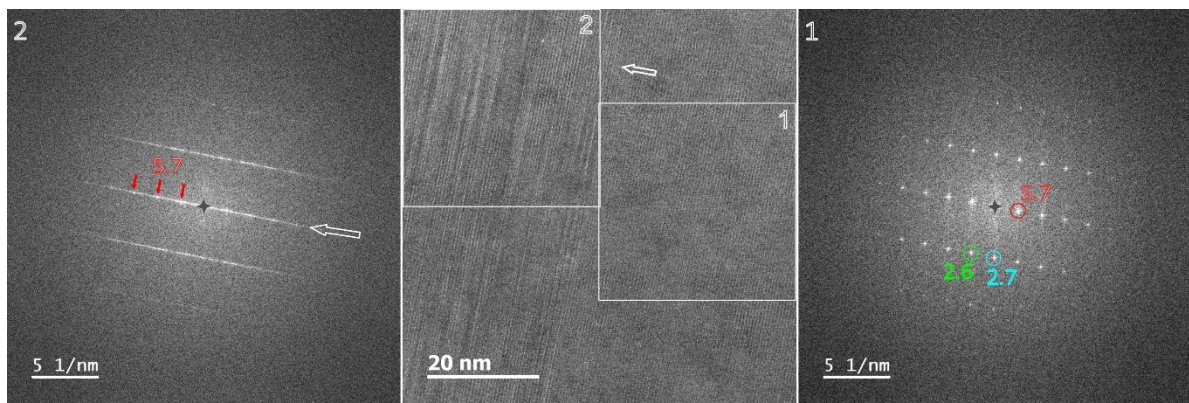Fig. 11 Medium resolution TEM image of a Cu_3TiO_z domain (area 6)

Fig. 12 High resolution TEM image of Cu_3TiO_z domain and Fast Fourier Transform of area 1 and 2, corresponding interreticular distances are given in Å. Notice the diffuse streaks along stacking direction (arrow) related to disorders in the periodicity on area 2.

As could be expected from area 6 SAED pattern (Fig. 10), the latter shows well defined dots, which correspond to the same interreticular distances. They correspond to α-Cu_3TiO_4 structure, trigonal polytype delafossite. The delafossite structure (ABO_2) can have two polytypes according to the orientation of the planar layer stacking. Hexagonal 2H types, that have a space group of $P6_3/mmc$, are formed when two A layers are stacked with each BO_2 layer rotated 180° in relation to one another, around the 6_3-fold axis passing through the A atom lines (Fig. 13). Alternatively, when the layers are stacked each layer in the same direction in relation to one another, it makes a rhombohedral 3R type with a space group of $R\bar{3}m$. In the Cu-Ti-O system, both polytypes can be stabilized, and the octahedral cation sites are mixed with half-Cu and half-Ti occupation, leading to the formulation $Cu(Cu_{1/2}Ti_{1/2}O_2)$ [23].

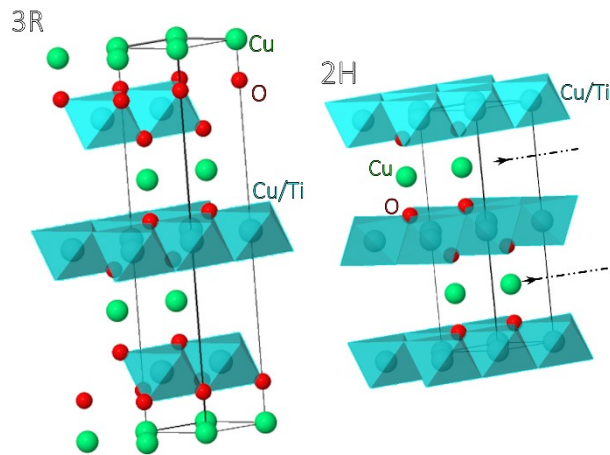Fig. 13 Perspective view of both 3R- and 2H- polytypes of the delafossite structure, α- and β-Cu_3TiO_4; arrows on 2H-type indicate the 6_3 fold axis of rotation of the planar ($Cu_{1/2}Ti_{1/2}O_2$) layers.

HAADF-STEM imaging allows to characterize the cation framework. Thus, considering the experimental HAADF-STEM images of this regular area and the simulated HAADF-STEM images of Cu_3TiO_4 structure, one is superimposed on the experimental one, it becomes clear that the regular area corresponds to the rhombohedral 3R type of delafossite structure, which might have been stabilized under the peculiar synthesis conditions at grain boundaries (Fig. 14).

The disordered areas, like the area 2 of domain 6, are characterized by frequent but irregular stacking change from 2H to 3R polytypes. From images, it appeared that 3R-type is preponderant in the Cu_3TiO_4 domains, in agreement with SAED patterns.
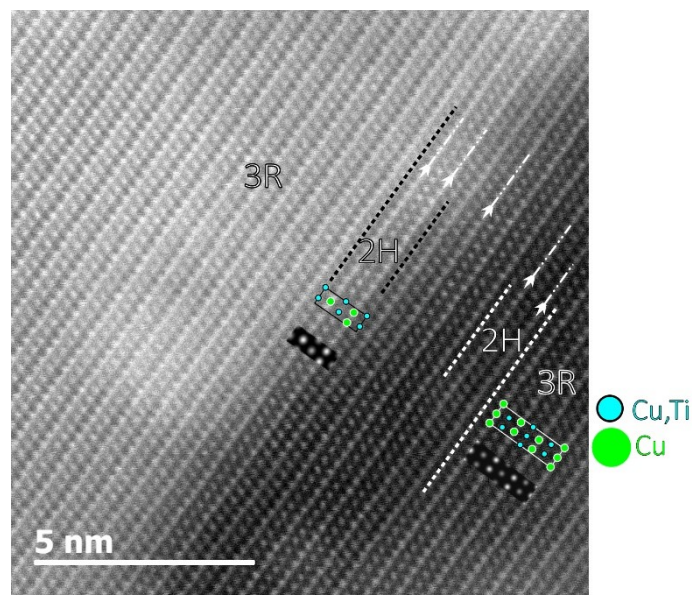

Fig. 14 HAADF-STEM image of an almost perfectly regular area 1 of domain 6; the simulated HAADF-STEM images are encrusted and the Cu site (big green) and mixed Cu-Ti octahedral site (small blue) are drawn on each Cu_3TiO_4 polytype unit cell, 2H- (black rectangle) and 3R- (white rectangle); white arrows indicate the 6_3-fold axis of the 2H -type. On left part of the image, a large 3R polytype area is observed.

d. EELS study results

EELS is a useful technique not only for identification of elements and quantification of local composition, but also for analysis of electronic structure (density of empty states, oxidation state, local coordination, bandgap….) [24]. It should be helpful to the identification of observed domains at the complex GB through the study of the oxidation and coordination states of copper from one domain to the other, which can be obtained from Electron Loss Near Edge Structure of core-loss Cu L-edge spectra. Table 2 gives the different expected copper environments.

Table 2. Summary of copper oxidation and coordination state in the different encountered structures at the GB

Structure	Oxidation state	Copper coordination state
$CaCu_3Ti_4O_{12}$	II	Square planar
CuO	II	Square planar
Cu_2O	I	Linear
Cu_3TiO_4	I	Linear (2 Cu)
	II	Octahedral (mixed Cu,Ti)

EELS data acquisition parameters are the following: STEM mode, convergence semi-angle 20mrad, collection semi-angle 55mrad, 0.05eV/ch dispersion, DualEELS mode including low-loss and copper $L_{2,3}$ core-loss region, energy resolution of 1eV deduced from full half-width of Zero-Loss Peak.

The peak positions of Cu $L_{2,3}$ white lines in Cu_2O and CuO (Fig. 15) are in complete agreement with the literature [25] and exhibit a shift to lower energy loss for the higher oxidation state. They confirm TEM observations (SAED, HREM and EDX) leading to the identification of area 8 (CuO) and 10 (Cu_2O) and will be used as internal spectrum references. As could be expected, the Cu $L_{2,3}$ white lines of CaCuTi fit well those of CuO spectrum, as well in energy position as for L_3/L_2 intensity ratio, corresponding to Cu^{2+}. In the same way, Cu $L_{2,3}$ white lines of core-loss Cu_3TiO_4 spectrum is a combination of CuO and Cu_2O spectra, with a stronger component of Cu_2O one in agreement with the $2/3Cu^{1+}$-$1/3Cu^{2+}$ repartition in Cu_3TiO_4 structure (Table 2).
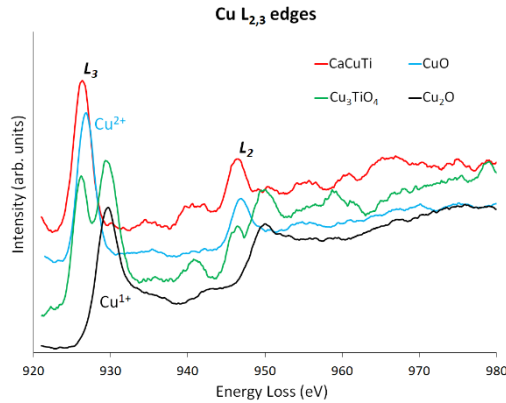
Fig. 15. Cu $L_{2,3}$ edges ELNES spectra of Cu_2O, Cu_3TiO_4, CuO and $CaCu_3Ti_4O_{12}$ (CaCuTi), normalized to the peak height

4. Conclusion

The material at the grain boundaries in polycrystalline $CaCu_3Ti_4O_{12}$ (CCTO) was structurally studied at the nanometric scale thanks to complementary scanning-transmission electron microscopy technics. Two different types of grain boundaries were isolated and characterized, simple GB and complex GB. The former, less than 2 nanometers thick, consist mainly in residual amorphous material containing traces of the synthesis precursor pollutants (Si, P, K). The latter, sitting at the boundary between at least three different CCTO domains, allowed the stabilization of three different phases: CuO, Cu_2O and delafossite-based Cu_3TiO_4, which form neighboring domains, of submicronic size. The coexistence of these different phases was shown, answering the question of what type of copper rich phase sits at the grain boundaries in CCTO ceramics. They should be considered when applying IBLC model to capacitance behavior of CCTO ceramics.

5. Acknowledgments

6. References

[1] M.A. Subramanian, L. Dong, N. Duan, B.A. Reisner, A.W. Sleight, High dielectric constant in $ACu_3Ti_4O_{12}$ and $ACu_3Ti_3FeO_{12}$ phases. J. Solid State Chem. 151(2) 323–325 (2000)

[2] A.P. Ramirez, M.A. Subramanian, M. Gardel, G. Blumberg, D. Li, T. Vogt, S.M. Shapiro, Giant dielectric constant response in a copper-titanate, Solid State Com. 115 217-220 (2000)

[3] C. C. Homes, T. Vogt, S. M. Shapiro, S. Wakimoto, A. P. Ramirez, Optical response of high-dielectric-constant perovskite-related oxide, Science, 293(5530) :673–676, (2001)

[4] B. Bochu, M. N. Deschizeaux, J. C. Joubert, A. Collomb, J. Chenavas, and M. Marezio. Synthèse et caractérisation d'une série de titanates pérovskites isotypes de $[CaCu_3](Mn_4)O_{12}$, J. Solid State Chem., 29(2) :291 (1979)

[5] S. M. Moussa, B. J. Kennedy, Structural studies of the distorted perovskite $Ca_{0.25}Cu_{0.75}TiO_3$, Mat. Res. Bull. 36(13-14):2525-2529 (2001)

[6] L. He, J. B. Neaton, M. H. Cohen, D. Vanderbilt. First-principles study of the structure and lattice dielectric response of $CaCu_3Ti_4O_{12}$, Phys. Rev. B, 65(21) :2141121 (2002)

[7] D.C. Sinclair, T.B. Adams, F.D. Morrison, A.R. West. $CaCu_3Ti_4O_{12}$: One-step internal barrier layer capacitor, Appl. Phys. Lett., 80(12) :2153–2155 (2002)

[8] T.B. Adams, D.C. Sinclair, and A.R. West, Giant barrier layer capacitance effects in $CaCu_3Ti_4O_{12}$ ceramics, Adv. Mat., 14(18) :1321 (2002)

[9] T-T. Fang and H-K. Shiau, "Mechanism for Developing the Boundary Barrier Layers of $CaCu_3Ti_4O_{12}$," J. Am. Ceram. Soc., 87, 2072–9 (2004)

[10] T.B. Adams, D.C. Sinclair, and A.R. West, "Characterization of Grain Boundary Impedances in Fine and Coarse-Grained $CaCu_3Ti_4O_{12}$ Ceramics," Phys. Rev. B., 73, 094124 (2006).

[11] R. Mauczok and R. Wernicke, "Ceramic Boundary-Layer Capacitors," Philips Tech. Rev., 41, 338–47 (1983).

[12] L. Marchin, S. Guillemet-Fritsch, B. Durand, A.A. Levchenko, A. Navrotsky, T.Lebey, Grain Growth-Controlled Giant Permittivity in Soft Chemistry $CaCu_3Ti_4O_{12}$ Ceramics. J. Am. Ceram. Soc., 91(2):485–489 (2008)

[13] V. Brizé, G. Gruener, J. Wolfman, K. Fatyeyeva, M. Tabellout, M. Gervais, F. Gervais, Grain size effects on the dielectric constant of $CaCu_3Ti_4O_{12}$ ceramics. Mater. Sci. Eng.: B 129, 135–138 (2006)

[14] G. Riquet, S. Marinel, Y. Bréard, C. Harnois, Sintering mechanism and grain growth in $CaCu_3Ti_4O_{12}$ ceramics. Ceram. Inter. 45(7): 9185-9191 (2019)

[15] T.B. Adams, D.C. Sinclair, A.R. West, *Decomposition Reactions in $CaCu_3Ti_4O_{12}$ Ceramics*, J. Am. Ceram. Soc. 89 (2006) 2833–2838.

[16] W. Yuan, Investigation on the decomposable process and the secondary liquid phase effect on the dielectric properties of $CaCu_3Ti_4O_{12}$ ceramics, J. Phys. D: Appl. Phys. 42 (2009) 175401.

[17] B.S. Prakash, K.B.R. Varma, The influence of the segregation of Cu-rich phase on the microstructural and impedance characteristics of $CaCu_3Ti_4O_{12}$ ceramics, J. Mater. Sci. 42:7467–7477 (2007)

[18] LA. Giannuzzi, F.A. Stevie, editors. Introduction to focused ion Beams. Instrumentation, Theory, techniques and Practice. New York: Springer (2005)

[19] Kirk E.C.G., D.A. Williams and H. Ahmed, Cross-sectional transmission electron microscopy of precisely selected regions from semiconductor devices, Inst. Phys. Conf. Ser. 100, 501 (1989).

[20] T. Yaguchi, T. Kamino, T. Ishitani, R. Urao, Method for Cross-sectional Transmission Electron Microscopy Specimen Preparation of Composite Materials Using a Dedicated Focused Ion Beam System, Microsc. and Microanal., 5(5) (1999) 365–370.

[21] P. A. Stadelmann, *JEMS – Electron Microscopy Software Java Version*; 2014-2018

[22] G. Riquet, PhD thesis (2019)

[23] K.J. Range und F. Ketterl, Preparation and Crystal Structure of α- and β-Cu_3TiO_4, Zeitschrift fuer Naturforschung B, 32 (1977) 1356-1357.

[24] R. F. Egerton, *Electron Energy-Loss Spectroscopy* (Springer,New York, 2011).

[25] Philip Ewels, Thierry Sikora, Virginie Serin, Chris P. Ewels and Luc Lajaunie, A Complete Overhaul of the Electron Energy-Loss Spectroscopy and X-Ray Absorption Spectroscopy Database: eelsdb.eu., Microsc. and Microanal., 22 (2016) 717–724, doi:10.1017/S1431927616000179.